Numerical and experimental investigations of Ti-6Al-4V chip generation and thermo-mechanical couplings in orthogonal cutting

Mahmoud Harzallah[a,*], Thomas Pottier[a], Johanna Senatore[a], Michel Mousseigne[a], Guénaël Germain[b], Yann Landon[a]

[a] Université de Toulouse, CNRS, Mines Albi, INSA, UPS, ISAE-SUPAERO; ICA (Institut Clément Ader), Campus Jarlard, F-81013 Albi, France
[b] Arts et Métiers ParisTech, LAMPA, 2 bd du Ronceray, 49035 Angers Cedex, France

Keywords:
Titanium alloy Ti-6Al-4V
Orthogonal cutting
Shear failure
High speed imaging
Fracture locus
Chip formation

A B S T R A C T

The chip formation mechanism of the Ti-6Al-4V remains a challenging problem in the machining process as well as its modeling and simulation. Starting from experimental observation on the titanium alloys Ti-6Al-4V machining shows that the ductile fracture in the chip formation is dominated by the shear phenomenon under high strain rate and temperature, the present work develops a new coupled behavior and damage model for better representation and understanding of the chip formation process. The behavior and damage of Ti-6Al-4V have been studied via hat-shaped specimen under temperature up to 900 °C and strain rate up to 1000 s^{-1}. An inverse identification method based on Finite Element (FE) is established in order to determine the constitutive law's parameters. The prediction of the segmented chip was analyzed through 3D finite element orthogonal cutting model which was validated by an in-situ and post-mortem orthogonal cutting machining observations. Finally, a particular attention is focused on the chip formation genesis which is described by three steps: Growth, Germination and Extraction.

1. Introduction

Machining is a common process that is widely used in the manufacturing of industrial parts. During the cutting process, the material is subjected to large strains at high strain rates which induce temperature increase (local heating) and a chip removal in complex conditions. The prediction of the process outputs (machined surface integrity, chip morphology and cutting forces) is an industrially and scientifically challenging task. Indeed the coupled nature of the phenomena requires setting up various models and often in a coupled manner. Moreover, the extreme velocity and temperature result in an additional difficulty related to models identification and validation.

Nowadays, thanks to significant advances in simulation techniques, various methods are used to enhance the quality of simulation predictions. Three main techniques were successfully used in previous studies: Finite Element (FE), Smoothed Particle Hydrodynamics, and Discrete Element Methods [1,2]. Among these techniques, the Finite Element Method is the oldest and was successfully implemented in various metals forming processes. It relies on a spatial discretization of the constitutive equations which may interact in a coupled manner.

The chip formation mechanism of many hard metals and especially Ti-6Al-4V, results in the generation of serrated chips. In such cases, the nature of the thermomechanical conditions drastically interlinks and therefore challenges the existing models. Many researchers addressed comprehensive and exhaustive studies on the physical phenomena involved in cutting such materials (adiabatic shear band, crack propagation) [3,4].

In order to describe the chip formation process, various published papers addressed constitutive behavior and damage laws which provide good descriptions for a wide range of materials concerning finite strain, strain rate and temperature-dependent visco-plasticity [5,6]. The Johnson Cook behavior model [7] is among these laws and is still the most popular phenomenological constitutive law adopted to model the material behavior during the cutting process [5,8,9]. Calamaz [10] has shown that within a tight range of strain rate and temperature the Johnson–Cook model is able to fit properly many metal forming processes. Unfortunately, outside of this range, the flow stress is known as poorly extrapolated.

Based on Johnson Cook approach [7], various researchers modified and/or extended the model to describe more accurately the flow behavior. These papers can be sorted into four groups.

The first group intended to modify the viscosity effect term. This term was the first to be changed by Holmquist and Johnson [11] to

* Corresponding author at: Ecole des mines d'Albi-Carmaux, Allée des sciences, Campus Jarlard, 81013 Albi CT Cédex 09, France.
E-mail address: mahmoud.harzallah@mines-albi.fr (M. Harzallah).

https://doi.org/10.1016/j.ijmecsci.2017.10.017

improve its impact at high strain rates by substituting it with a simple power law. Rule and Jones [12] modified this term to better describe the rapid increase of the stress around 10^3 s^{-1} in the case of copper and aluminum samples. Finally, a quadratic formulation was added to this term by Woo Jong Kang [13] to enhance the strain rate sensitivity effect for various sheet steels.

Modifications of the hardening term were addressed by Tan et al. [14] for 7050-T7451 alloy in uniaxial isothermal tensile tests. The authors proposed a revised Johnson–Cook model by introducing a coupling between hardening and strain rate through hardening coefficients. Based on experimental observations, Khan et al. [15] proposed an alternate formulation of the same coupling to describe the quasi-static and dynamic behavior in the case of titanium alloy Ti-6Al-4V. By considering a strong effect of the thermal softening on the strain hardening, a revised Johnson–Cook model was proposed by Vural and Caro [16] which provided a good correlation with the experimental data.

The third group focused on the thermal term. Inspired from Johnson–Cook model, several formulations were proposed by Lin et al. [17] considering the coupling effects between the strain, strain rate and temperature on the flow stress. Li et al. [18] proposed a new formulation which considers the coupling between strain and temperature at high strain rate on the flow behavior in the case of a hot compression of T24 steel. For machining process, Bäker [19] modified the Johnson–Cook model by considering a strong coupling between the hardening and the thermal softening phenomena in order to describe the dominance of this latter at high temperatures. A loss of ductility was observed by Sartkulvanich et al. [20] in the case of the AISI 1045 in a temperature range between 200 °C and 400 °C. The authors modified the Johnson–Cook thermal term by adding an exponential formulation to reproduce this effect.

Finally, many extensions of the Johnson–Cook flow stress model were proposed by the fourth group. The first extension was added through a multiplicative term by Andrade et al. [21] to describe the decrease of the stress caused by the dynamic recrystallization in the case of copper compression tests at a strain rate of 10^{-3} s^{-1}. To improve physical understanding of the chip formation during the cutting process, an extension known as *Tanh* term was proposed by Calamaz et al. [10] and used by Sima and Özel [22] in order to describe the strain softening phenomenon effects at high temperature in titanium alloys.

In the present study, the focus on serrated chips has led to pay a special attention to the damage model. Indeed, material separation in such thermomechanical conditions involves complex physical mechanisms.

Because of the widespread applications involving large plastic deformations accompanied by rapid increase of temperature and damage evolution, many works were devoted to ductile fracture.

McClintock [23] and also Rice and Tracey [24] proposed a theory based on the growth of cylindrical and spherical voids the model fracture. Porosity based fracture theories such as developed by Gurson [25] is another microstructure based model. On the other hand, phenomenological approaches have also been proposed by Cockcroft and Latham [26] and many others since then.

Most of these models exhibited a high dependency to the stress triaxiality. In fact, based on experimental observations, many researchers showed the major impact of the hydrostatic pressure. Using round bar specimens, Bridgman [27] was the first to analyze the strain failure sensibility to the hydrostatic pressure in the neck of specimen. Under hydrostatic loading, Rice and Tracey [24] described the growth of voids and cavities by a simple exponential expression as a function of the stress triaxiality η. Especially, Rice and Tracey's expression became very popular in the fracture application and various researchers extended or modified the model to study the damage evolution. Johnson and Cook [28] extended this expression by considering separately the strain rate sensitivity and temperature dependency, which allowed a broad application of this model in a wide array of thermomechanical processes [5,8]. However, the work of Wierzbicki et al. [29] proved that the approximation of the failure strain with a monotonically decreasing function of stress triaxiality is poor, while a strong dependency to the third stress invariant is to be preferred. Wilkins et al. [30] were the first to introduce separately the deviatoric stress and the Lode angle effects in their damage model. As an extension of Wilkins' model and Johnson–Cook's model, Wierzbicki and Xue [31] postulated a new formulation by introducing the dependency to these two variables.

It can be mentioned that the dependency in temperature and strain rate is not explicitly addressed in the majority of damage models. By contrast, it is implicitly presented through their behavior law as a thermo-visco-plastic evaluation of stress.

The present paper firstly, proposed and details a new formulation of Johnson Cook model through its Ludwick hardening term. Its experimental identification through hat-shaped compression tests at various temperature and strain rate is then presented. Validation is performed through a comparison with the Johnson Cook model. Secondly, a modified Max shear damage model and its calibration are detailed. Then, by means of 3D FE orthogonal cutting model, the chip formation process is investigated and compared to experimental observations. These latter are performed in-situ, during the cutting process and either at high magnification and high frame rate. The chip length, height, angles and frequencies are used for comparison purpose. The comparison to recorded cutting forces is also presented. Finally a comprehensive discussion on the chip generation phenomenon is addressed.

2. Flow rule and parameter identification

2.1. Model description

The main goal of the proposed modeling is to prevent from an always controversial model selection process by assuming the simplest model for hardening namely the Ludwik's law [32] which is a restriction of the Johnson Cook model. The coupling in strain-rate and temperature is then permitted through material parameters. The flow stress thus becomes:

$$\sigma = A(\dot{\varepsilon},T) + B(\dot{\varepsilon},T).{\varepsilon_p}^{n(\dot{\varepsilon},T)} \tag{1}$$

where $A(\dot{\varepsilon},T)$, $B(\dot{\varepsilon},T)$ and $n(\dot{\varepsilon},T)$ are respectively the yield strength, the hardening modulus and the hardening coefficient. These parameters exhibit a dependency on both the strain rate and temperature.

2.2. Mechanical tests

The parameter identification is performed through nine dynamic tests using hat-shaped specimen loaded in compression by a Gleeble 3500 testing machine. Various speed and temperature are investigated, ranging from 10^{-1} mm s^{-1} to 10^3 mm s^{-1} and from 20 °C to 900 °C respectively. These tests were performed by Germain et al. [33]. Raw force/displacement curves are plotted in Fig. 1.

As shown in Fig. 1, the force is affected by both temperature and strain rate (since the proportionality between the crosshead speed and strain rate is assumed). As expected, the force decreases with temperature and increases with the strain rate. Particularly, a small effect of the strain rate at ambient temperature is observed between 10^{-1} mm s^{-1} and 10^2 mm s^{-1}.

2.3. Model calibration procedure

The main advantage of the formalism proposed in Eq. (1) is that it does not presume any shape for the couplings, and users can fit their experimental points by any suited analytical function. Though a minimum of three tests are required to fully calibrate the proposed model, the explicit nature of the coupling leads to a direct relation between the identification quality and the amount of calibration tests, whereas it is not necessarily true if the interpolant shape is set a priori (e.g. the Johnson–Cook model).

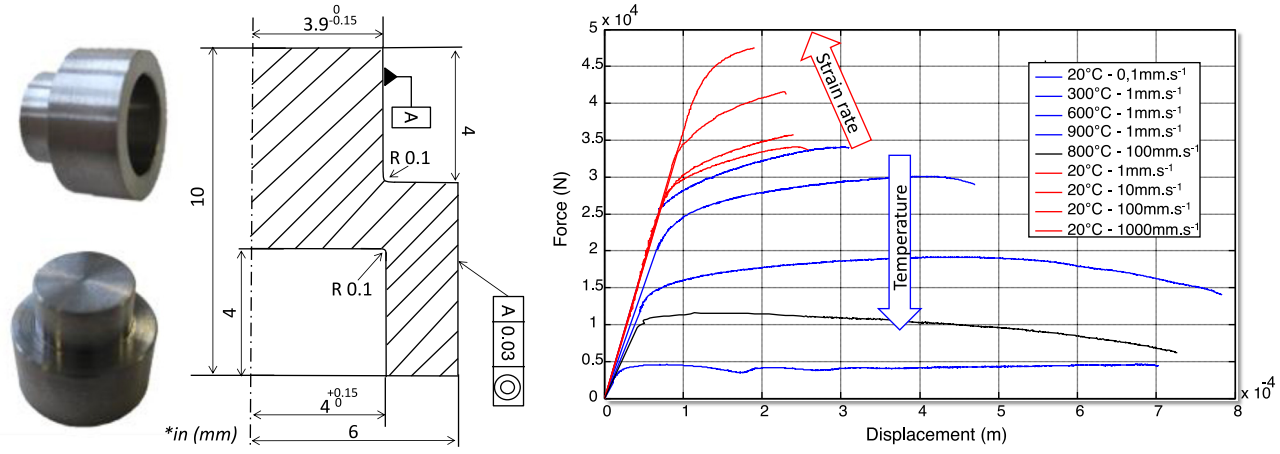

Fig. 1. (a) Hat-shaped specimen geometry (mm); (b) Experimental force–displacement curves of titanium alloy Ti-6Al-4V.

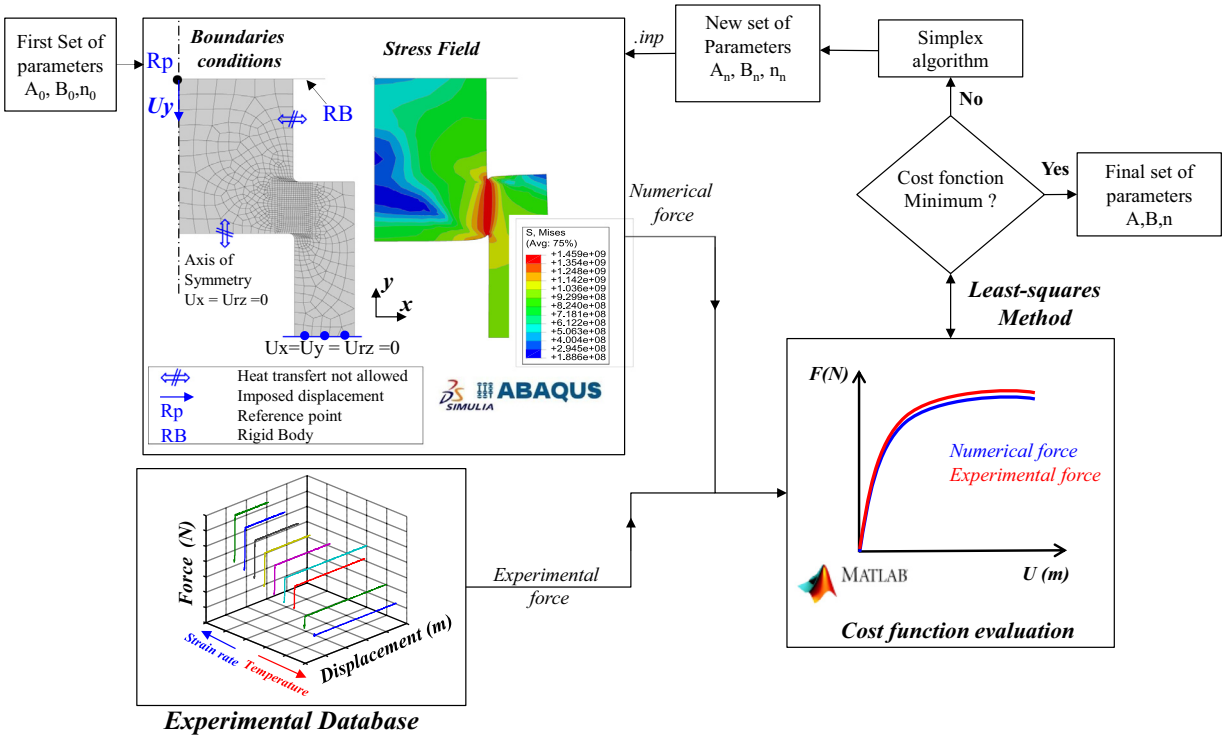

Fig. 2. Iterative solving flowchart of the inverse problem.

Moreover, the univocal aspect of the calibration procedure ensures that a set of tests leads to a one and only parameter set. On the contrary, in the case of the Johnson–Cook model (and its by-product) several parameter sets can be obtained from the same measured data depending on which order is chosen for the identification (strain-rate term first or temperature term first).

The hat-shaped tests have already been used for analytical identification [34]. However, such procedure relies on several coarse assumptions such as: (i) rectangular region of interest (ROI), (ii) rigid body behaviors outside of the ROI, (iii) homogeneity of the strain rate over the material and (iv) stress uniaxiality. The strictness of such hypothesis led various authors like Germain et al. [33] to consider inverse identification in such cases and these studies proved this choice worthy. In the present paper, finite elements update (FEU) is used to retrieve material parameters from force mean square comparison and a simplex optimization algorithm. More details on the FEU approach can be found in Harzallah et al. [35]. The different steps of numerical implementation are summarized in Fig. 2.

An axisymmetric finite element hat-shaped model is developed on ABAQUS Explicit platform. The sample is meshed by quadrilateral axisymmetric elements, coupled in temperature–displacement in reduced integration calculation (CAX4RT). Both the moving and fixed compression plates are modeled as analytical rigid bodies which are tied to the sample.

The iterative solving procedure leads to a simultaneously optimized parameter set (*A, B, n*) for each of the nine tests at various strain-rates and temperature. On Fig. 3, these identified parameters are plotted as black dots.

The obtained parameter sets allow to introduce the suited analytical description of the thermo-visco-plastic coupling. It can be seen from Fig. 3 that plane fitting of the all three parameters within the temperature-strain-rate space properly approximates the experimental data.

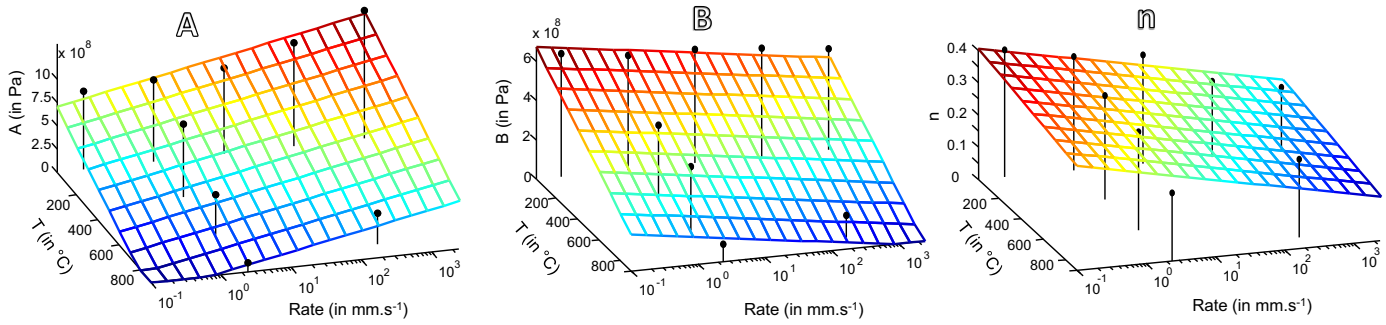

Fig. 3. Modeling of the coupling for A, B and n. The best fit of each experimental response are plotted as black dots.

Table 1
Identified flow rule parameters for Ti-6Al-4V.

	A (Pa)	*B* (Pa)	n
a	9.36e + 005	5.57e + 05	9.46e−05
b	−1.45e + 08	4.66e + 07	4.23e−02
c	−8.65e + 08	−6.39e + 08	−0.365

Table 2
The identified Johnson–Cook parameters.

A (MPa)	*B* (MPa)	*C*	*n*	m
880	582	0.041	0.353	0.6337

Based on these observations, the evolution of the parameters as a function of temperature and strain rate is described by planes. For each parameter, the plane equation is expressed as (Eq. 2):

$$A, B, n = -\boldsymbol{a}.T - \boldsymbol{b}.\log(\dot{\varepsilon}) - \boldsymbol{c} \tag{2}$$

where *a, b* and *c* are the constitutive parameters of the law. These values are reported in Table 1.

2.4. Comparison with the Johnson–Cook model

In order to assess the improvement brought by the proposed model, a comparison with the Johnson–Cook constitutive law is performed. In fact, this latter model describes the flow stress of materials as a multiplication of three terms: hardening term of Ludwick [32], viscosity (strain rate) and thermal dependency (Eq. 3).

$$\sigma = \left[A + B\left(\varepsilon_p\right)^n\right]\left[1 + C\ \mathrm{Log}\left(\frac{\dot{\varepsilon}_p}{\dot{\varepsilon}_{p0}}\right)\right]\left[1 - \left(\frac{T - T_r}{T_m - T_r}\right)^m\right] \tag{3}$$

where $\varepsilon_p, \dot{\varepsilon}_p, \dot{\varepsilon}_{p0}$ are respectively the plastic strain, the strain rate and reference plastic strain rate and T, T_r,T_m are the temperature, the room temperature, the melting temperature of the workpiece material. *A, B, C, m, n* are material parameters to be calibrated. For this task, the same FEU identification procedure applied earlier for $A(\dot{\varepsilon}, T)$, $B(\dot{\varepsilon}, T)$ and $n(\dot{\varepsilon}, T)$ and presented in Fig. 2, is used again to identify the 5 parameters of the Johnson Cook at once. A Levenberg–Marquardt algorithm [36] was used for a simultaneous identification of the set of parameters (*A, B, C, m, n*) over the whole experimental database at once (i.e. the 9 tests). This latter algorithm is proven worthy when the number of parameters became consequent [37]. In addition, the quality optimal solution was verified by checking that the same optimum set is reached from various initial set of parameters. The identified Johnson–Cook parameters are mentioned in Table 2.

The optimum set of parameters for the two models (the proposed one and J-C) are used in a finite element simulation of every hat-shaped compression tests. This allows obtaining numerical loading forces along with the corresponding displacements. Both models are compared to experimental data for various temperature and strain rate (Fig. 4).

It can be seen that despite the plane approximation, the proposed model properly predicts the experimental data and gives better results than the Johnson–Cook model under all conditions. Because of the constant parameters of the hardening term in the Johnson–Cook law, the shape of the hardening curves remain the same over all conditions and such hypothesis is here proven quite erroneous.

At ambient temperature (20 °C), the proposed model properly fits the experimental behavior while the Johnson–Cook model shows an acceptable error. But within the wide range of temperature and strain rate covered in this application, the error increases as a function of these phenomena for both models. Nevertheless the magnitude of this error remains smaller for the proposed model than for the JC model.

3. Damage model implementation

After calibration and validation of the proposed behavior law, a particular attention is paid to the damage model through the coupling between phenomena in the chip formation process.

The experimental observations performed by Pottier et al. [38] proved that a ductile fracture occurs during the machining process that is caused by extensive plastic deformation induced by the shear phenomena in the material. From a micromechanical stand point, it is related to nucleation, growth and coalescence of void provoked by the increase of the density of dislocations under high temperature and strain rate. From a phenomenological stand point, the ductile fracture is described as an accumulation of plastic shear strain induced by the process. The damage modeling classically relies on a cumulative formulation of the damage internal variable *D*, of which the evolution throughout plasticity is defined by (Eq. 4)

$$\dot{D} = \frac{d\varepsilon_p}{\bar{\varepsilon}_f} \tag{4}$$

Such formalism requires the assessment of the strain at failure: $\bar{\varepsilon}_f$. Various relations to the mechanical fields were developed for this purpose. However, the shear nature of the loading and the narrow range or stress triaxiality involve in cutting have led to consider max shear failure criterion as suited for this study. The strain rate and temperature dependency is thus being addressed through the material parameters as proposed in the above for the hardening law.

3.1. The maximum shear (MS) damage criterion in the spherical coordinate system $(\bar{\varepsilon}_f, \eta, \theta)$

The maximum shear (or Tresca) damage criterion can be expressed in terms of principal stresses by Eq. (5).

$$\sigma_1 - \sigma_3 = 2\tau_f \tag{5}$$

where τ_f, is the only parameter to calibrate and stands for the maximum shear stress at failure.

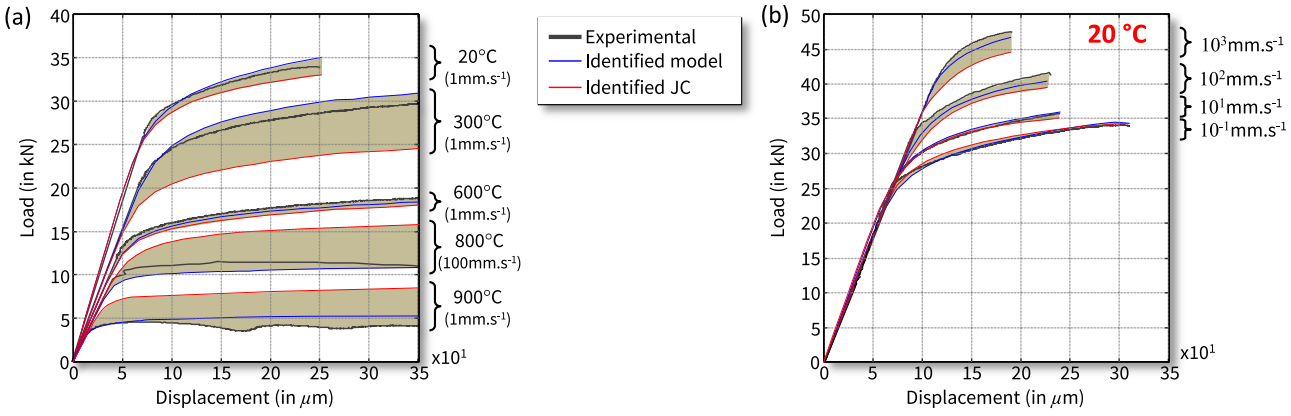

Fig. 4. Comparison between experimental data, proposed model and Johnson–Cook model curves under: (a) Temperature (b) Strain rate.

From geometrical consideration the maximum shear damage criterion can be transposed within the $(\bar{\varepsilon}_f, \eta, \theta)$ space from Eq. (6).

$$\begin{cases} S_1 = \frac{2}{3}\bar{\sigma}\cos\theta \\ S_2 = \frac{2}{3}\bar{\sigma}\cos\left(\frac{2\pi}{3} - \theta\right) \\ S_3 = \frac{2}{3}\bar{\sigma}\cos\left(\frac{4\pi}{3} - \theta\right) \end{cases} \tag{6}$$

where $\bar{\sigma}$ is the second stress invariant, θ is the lode angle and the S_i are the principal component of the stress deviator tensor. More details on these transformations can be found in references [39,40].

Through equations (6), an expression of the three principal stresses can straight-forwardly be obtained as a function of $\bar{\sigma}, \theta$ and σ_m the first invariant as follows:

$$\begin{cases} \sigma_1 = \sigma_m + S_1 = \sigma_m + \frac{2}{3}\bar{\sigma}\cos\theta \\ \sigma_2 = \sigma_m + S_2 = \sigma_m + \frac{2}{3}\bar{\sigma}\cos\left(\frac{2\pi}{3} - \theta\right) \\ \sigma_3 = \sigma_m + S_3 = \sigma_m + \frac{2}{3}\bar{\sigma}\cos\left(\frac{4\pi}{3} - \theta\right) \end{cases} \tag{7}$$

By introducing these expressions of σ_1 and σ_3 into the maximum shear criterion (Eq. 5), the model can be expressed as a function of the normalized lode angle by (Eq. 8):

$$\bar{\sigma} = \tau_f \left[\frac{1}{\sqrt{3}} cos\left(\frac{\pi}{6} - \bar{\theta}\right)\right]^{-1} \tag{8}$$

With $\bar{\theta} = 1 - 6\theta/\pi$. However, damage criteria are usually described and implemented though the equivalent strain at failure $\overline{\varepsilon_f}$. For that purpose, Eq. (8) is used to modify the coupled Ludwick's flow law presented in the above. The coupled parameters *A, B*, and *n* identified previously are reused to enrich the damage description and dependency to both temperature and strain-rate. The maximum shear damage criterion therefore provides an expression of the equivalent strain at failure as a function of not only θ and τ_f but also as function of T and $\dot{\varepsilon}$ such as (Eq. 9):

$$\overline{\varepsilon_f} = \left[\frac{\sqrt{3}\,\tau_f}{B(\dot{\varepsilon},T).\cos\left(\frac{\pi\bar{\theta}}{6}\right)} - \frac{A(\dot{\varepsilon},T)}{B(\dot{\varepsilon},T)}\right]^{\frac{1}{n(\dot{\varepsilon},T)}} \tag{9}$$

However, Bai and Wierzbicki [40] shown that only the plane stress condition enable to relate between triaxiality and the Lode angle (Eq. 10).

$$cos(3\theta) = \cos\left[\frac{\pi}{2}(1-\bar{\theta})\right] = -\frac{27}{2}\eta\left[\eta^2 - \frac{1}{3}\right] \tag{10}$$

It can be mentioned that only one additional parameter needs to be calibrated, namely the maximum shear stress at failure τ_f. It can be identified from any kind of tests of known load angle, through the principal stresses at the point of fracture and should also depend on strain rate and temperature $\tau_f = \tau_f(\dot{\varepsilon}, T)$ see reference [29].

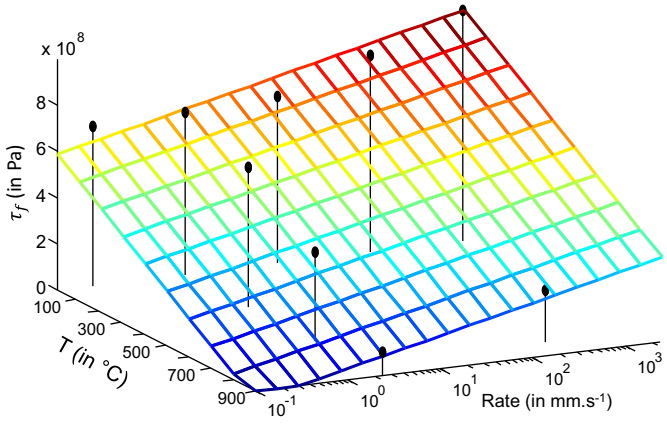

Fig. 5. The $\tau_f(\dot{\varepsilon}, T)$ parameter identified evolution (black dots) and its least square plane fit in the temperature/strain-rate space.

Table 3
The identified parameters of τ_f.

	a	b	c
τ_f	$7.17.10^5$	$-9.3.10^7$	$-6.96.10^8$

3.2. MS damage criterion calibration

As recommended by Wierzbicki et al. [29], the choice of shear tests with $\bar{\theta} = 0$ ease the identification process. For that reason, experimental values of the shear stress at failure are obtained from the hat-shaped tests presented above. Inverse identification is performed to obtain the stress fields corresponding to the global displacement observed at failure. The stress fields are obtained from the identified flow model.

The obtained values of $\tau_f(\dot{\varepsilon}, T)$ are shown in Fig. 5 and the parameters of the fitting least-square plane are summarized in Table 3. Accordingly, this parameter is described as a function of temperature and strain rate through Eq. (2).

The shape of the fracture locus is presented in Fig. 6a for a given temperature and strain rate. The strain at failure value, which used for calibration, is determined from the optimized hat-shaped numerical simulation under the corresponding loading conditions. It can be seen that direct dependency to the stress triaxiality ratio η is not shown, however this coupling is derived from the coupled nature of the load angle and η. By means of Eq. (10), this point is highlighted in Fig. 6b in the case

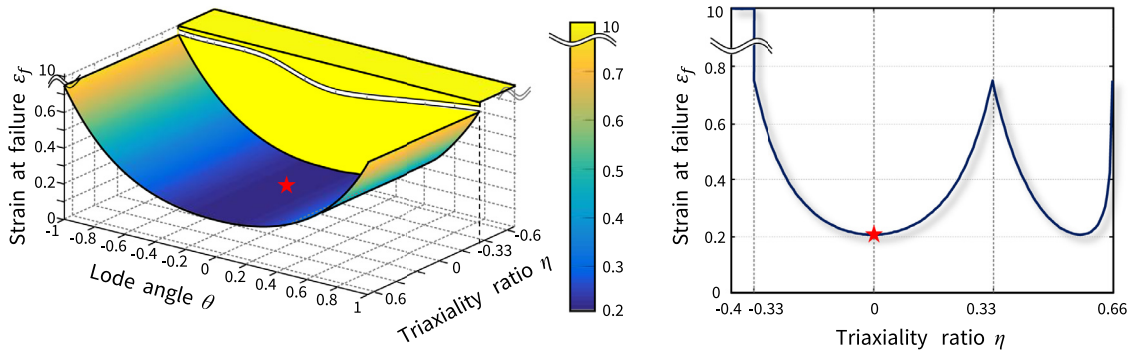

Fig. 6. (a) Shape of the identified fracture locus in the $(\bar{\varepsilon}_f, \eta, \theta)$ space at $T = 20$ °C and a rate of 1 mm s^{-1}. (b) Restriction to the plane stress case. The calibration point is depicted as a red star ($\varepsilon_f = 0.213$). (For interpretation of the references to color in this figure legend, the reader is referred to the web version of this article.).

of plane stress hypothesis, where the fracture locus clearly depends on η.

In addition, as mentioned by Bao and Wierzbicki [41], for low triaxiality, the nature of metallurgical phenomenon related to damage changes, so that cracks can no longer propagates due to high compressive stress state, which leads to experimental observations where material is clearly affected but exhibits no failure. For this purpose, the value of the strain at failure is set to 10 when the loading triaxiality ratio decreases below $\eta_{sat} = -1/3$.

4. Chip formation simulation

By the means of ABAQUS/Explicit and user material subroutine VUMAT, the damage and behavior models are implemented into a 3D-orthogonal cutting FE model.

In addition to these two constitutive laws, the simulation of the chip formation process also requires a good control and description of many parameters: (i) parts geometries, (ii) boundary conditions, (iii) friction evolution.

4.1. Initial geometry, meshes and boundary conditions, and material properties

Thermomechanical fields are calculated from the use of 3D continuum elements under reduced integration (C3D8RT). Mesh is refined in the region of interest in order to enhance the accuracy at the tool tip. The lowest mesh size in the model is about 25 µm while the coarsest is (200–500 µm).

The tungsten carbide tool is considered as deformable and modeled by a thermo-elastic law. It has an edge radius of 20 µm, a clearance angle of 11° and two rake angles are tested namely −5°, 15°.

The dimensions of the workpiece are 10 mm in length, 1.5 mm in width ($w = 3$ but a plane of symmetry is defined) and 1.7 mm in height. It is modeled by a single partition to avoid many modeling hypotheses. That favors the chip separation and helps to be more realistic.

As summarized in Fig. 7, nodes on the back surface of the tool are locked over 6 dof. The bottom surface of the workpiece is only free to translate along the X axis. The displacement of the nodes on the back surface of the workpiece is imposed with a constant velocity that equals the desired cutting speed.

The 3D finite element model is setup under symmetric condition (Fig. 7) in order to investigate the evolution of damage mechanism either under plane strain assumption (center of the chip $y = w/2$) and plane stress assumption (side free surface $y = 0$).

4.2. Contact and friction modeling

Another important feature of finite element based computation in cutting simulation is the friction law. It is influenced by many factors such as sliding velocity, local contact pressure, temperature, tool and workpiece materials as proven by Ben Abdelali et al. [42]. Due to its simplicity and its availability in all FE codes such as Abaqus [43], the Coulomb friction model is commonly used for this application as done by Bäker [19]. Extensive studies were carried out at the tool/chip interface by Puls et al. [44] which are shown a strong material adhesion at the tool tip vicinity. When moving along the rake face, a sliding motion of the chip was observed.

Accordingly, a *stick-slip* friction model was developed by Zorev [45]. It advocates the existence of two distinct contact regions (Fig. 8): sticking contacts around the tool tip where the shear stress τ_f is assumed to be equal to the yield shear stress of the material, τ_y , whereas, in the sliding region, the frictional stress is lower than the yield shear stress. Based in these assumptions, a Coulomb–Tresca model is adopted to define the tool–chip interface contact which is described as follows (Eq. 11):

$$\begin{cases} If\ \tau_f < \tau_y\ \ then\ \tau_f = \mu.\sigma_n \text{ (Sliding region)} \\ If\ \mu.\sigma_n = \tau_y\ \ then\ \tau_f = \tau_y \text{ (Stick region)} \end{cases} \tag{11}$$

where σ_n is the normal stress and μ the Coulomb's friction coefficient is here set to 0.2 as proposed by Zhang et al. [46].

4.3. Materials, machining parameters and contact conditions

The physical properties of the tool and the workpiece, as well as the contact conditions are reported in Table 4, whereas the constitutive and damage model parameters are mentioned above in Table 1.

5. Results and discussion

The present section deals with the numerical and experimental results obtained from orthogonal cutting of titanium alloy Ti-6Al-4V. In order to validate the orthogonal cutting model developed in the present work, the numerical results are compared to experimental data. The evolutions of the chip size and cutting forces are thus monitored and compared. Moreover, a particular attention is paid to the chip morphology in terms of segmentation and the physical mechanism governing the particular chip shape generation.

5.1. Finite element chip morphology results

The simulations carried out are presented in Fig. 9. The damage distribution corresponding to material degradation during the chip formation process is presented for four machining conditions in terms of cutting speed (15 and 25 m min^{-1}) and rake angle (−5° and +15°).

Under all machining conditions, segmented chip morphology and quasi-periodic cracks are observed. The material separation initiates at the side free surface, close to the tool tip and propagates within the material. It can be noticed that most of the damage phenomenon is localized at the tool–chip interface (secondary shear zone) and in the shear band

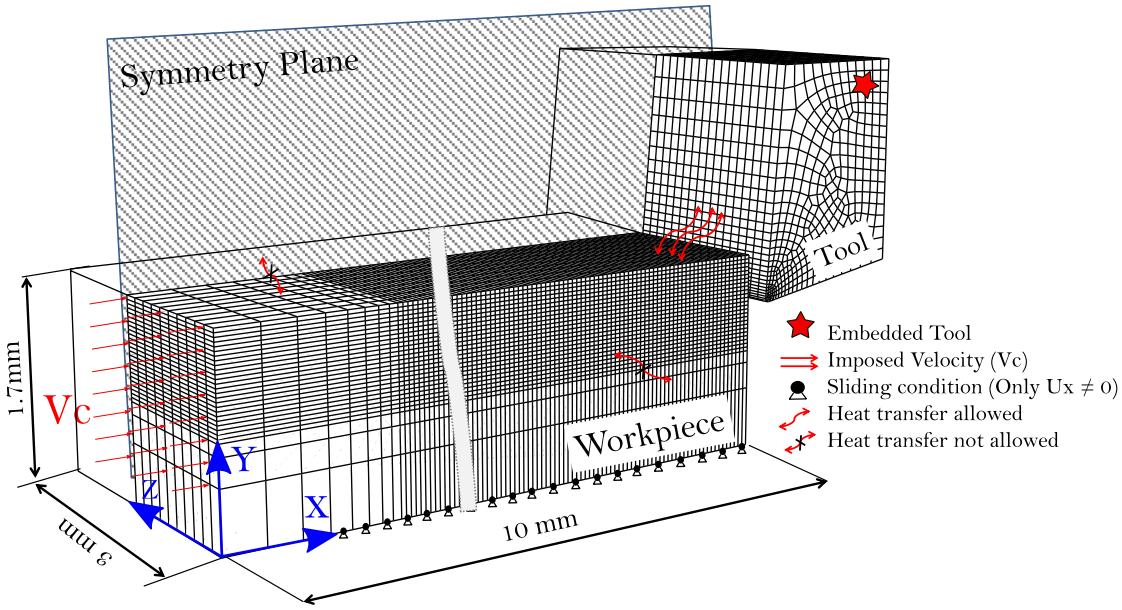

Fig. 7. Orthogonal cutting model: geometries and boundaries conditions.

Table 4
Material properties and contact condition.

Material properties and contact conditions [5]			
Materials properties	Property	Workpiece	Tool
	Density ρ (kg m^{-3})	4430	15,700
	Elastic modulus E (GPa)	110	705
	Poisson's ratio ϑ	0.33	0.23
	Specific heat C_p (J kg^{-1} °C)	670	178
	Thermal conductivity λ (W m^{-1} °C)	6.6	24
	Expansion coefficient $\alpha_{expansion}$ (μm m^{-1} °C)	9	5
	Room temperature T_{room} (°C)	20	
	Inelastic heat fraction β_{TQ}	0.9	–
Contact	Friction coefficient μ	0.2	
	Friction energy transformed to heat	99%	

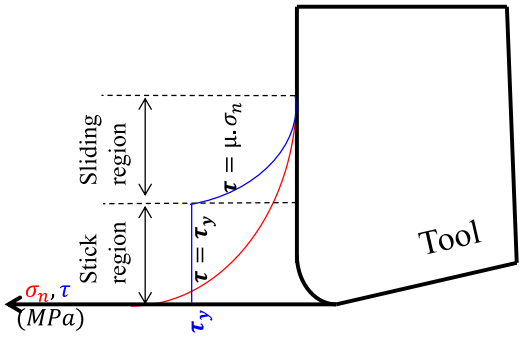

Fig. 8. Stick-slip contact Model.

(primary shear zone). The segments morphology is greatly affected by the rake angle while the cutting speed seems of least influence. These observations are to be confirmed by experimental comparison and this is the point of the next section.

5.2. Experimental setup

One of main improvement of this work is the use of high speed camera equipped by a high magnification optics allowing to access the region of cut and therefore to observe and analyze the chip formation mechanisms.

The orthogonal cutting configuration is obtained through a specific test devise (DEXTER) developed for this application. The relative speed between the tool and the workpiece is obtained using a linear axis which allows varying the cutting velocity up to 120 m min^{-1}. The uncoated carbide tools (rake angles $\gamma = -5°$; $+15°$) are fixed on a 6-components dynamometer (Kistler 9257A) in order to measure the force components for each cutting configuration.

The workpiece is polished and etched for 10 s by kroll's reagent to reveal Ti-6Al-4V microstructure, thus permitting a better accuracy in the image analysis. A depth of cut of 0.25 mm is selected and two cutting speeds were investigated (15 and 25 m min^{-1}).

The optical device (Fig. 10) consists of a Photron SA3 camera with CMOS sensor, coupled to a reflective Schwarzschild objective (magnification X15). A 120 W halogen light guide is used to illuminate the scene.

The use of high speed camera requires a compromise between frame rate, frame resolution and the cutting velocity in order to obtain acceptable images (unblurred). Consequently, these parameters are modified for the tests as highlighted in Table 5. These settings ensure a pixel size of 1.133 μm/pixel.

5.3. Chips morphology

All the performed cutting tests led to serrated chips, generated from periodic cracks propagation (Fig. 11). It is also found that the chip morphology differs whether positive or negative rake angles are used.

It must be mentioned that a significant transversal (out of plane) deformation of the chip surface is observed for all cutting conditions. As

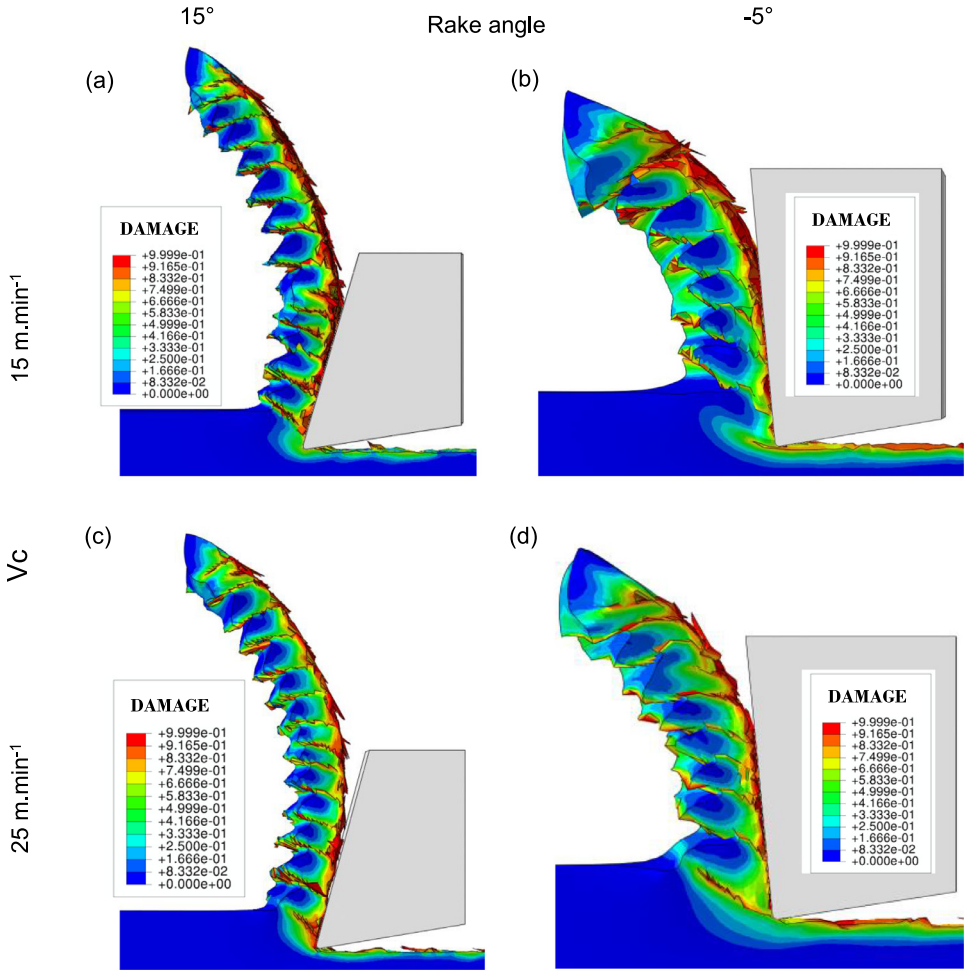

Fig. 9. Numerical results under all machining parameters.

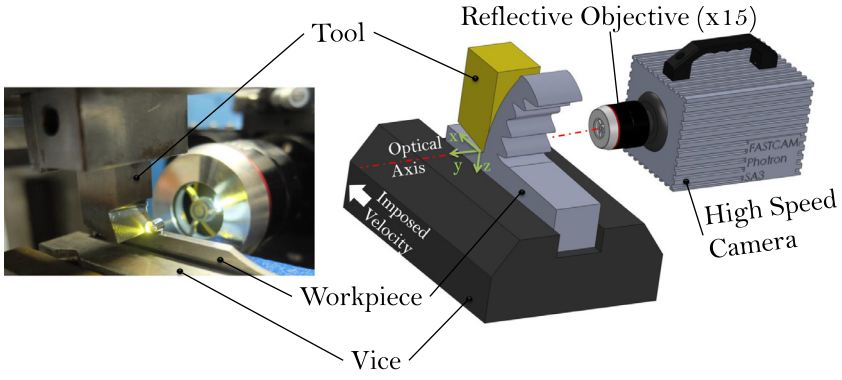

Fig. 10. Experimental setup.

Table 5
Machining and recording parameters.

	Rake angle (°)	Cutting velocity (m min^{-1})	Frame rate (fps)	Spatial resolution (pixels)	Exposure time (μs)
Test 1	15	15	6000	512×512	5
Test 2		25	10,000	384×352	2.5
Test 3	−5	15	6000	512×512	4
Test 4		25	10,000	384×352	2.5

Table 6
Number of frames and segments for each test.

Test number	Number of frames	Number of measured segments	Metric frequency of segmentation (segment/mm)
1	2113	306	2.49
2	1166	362	3.26
3	1761	161	2.15
4	2049	251	2.89

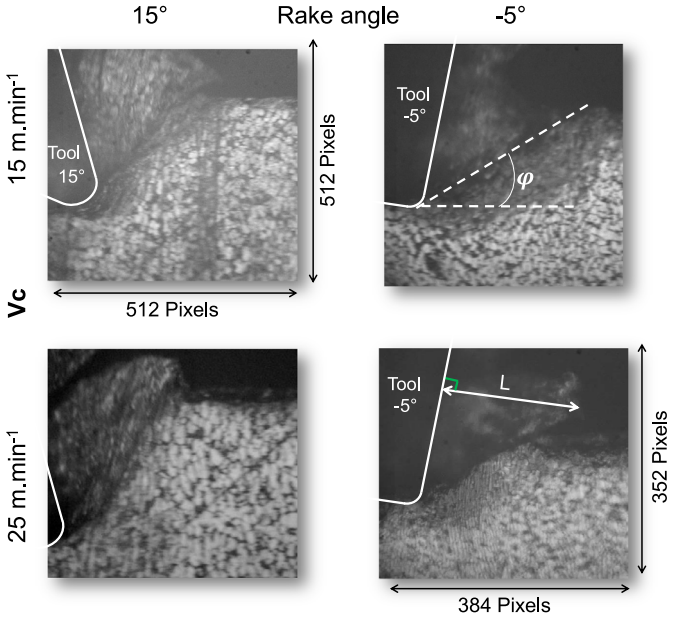

Fig. 11. Images captured at four cutting conditions and geometrical parametrization of the chip morphology.

depicted in Fig. 12, further altimetry investigations by extended field confocal microscopy (EFCM) showed that the magnitude of this deformation increases with negative rake angles. A significant swell is observed in the secondary shear zone and more specifically in the stick region (see Section 4.2). Another bulge is observed atop the segment. This corresponds to the tertiary shear zone of the previous cut. The magnitude of this deformation doubles when the rake angle ranges from 15° to −5°. This latter finding leads to consider that such angles affect more deeply and more significantly the generated surface. However further investigations need to be conducted to be conclusive on this matter.

Thanks to fast imaging technique, the serrated chip morphology can be analyzed more in details and characterized by their length (L) and the shear angle (φ) as defined in Fig. 11. These parameters were measured for each segment of each test in order to investigate the evolution of the chip shape regarding the rake angle and the cutting velocity.

The whole captured sequence for each test is described by its number of frames and the corresponding number of segments, as summarized in Table 6.

To analyze the chip segmentation phenomenon, many parameters are defined in the literature, such as the chip segmentation frequency (Hz) and the segmentation intensity [47,48]. However, these latter are not able to ensure comparison with other tests under different machining conditions. Consequently, in the present work, the characterization of the metric frequency of segmentation (in segment per millimeter) is preferred.

As it can be seen in Table 6, the metric segmentation frequency strongly depends on cutting conditions. It increases with both the cutting speed and the rake angle. This parameter is directly linked to the segment length, but may also be influenced by the shear angle. Fig. 13 depicts the distributions and evolutions of the segments lengths and the shear angles.

It can be seen from Fig. 13a, c, e and g that the experimental segment length distributions seem to be normally distributed and exhibit a strong dispersion for all tests. By comparing with numerical results, the average value of the segment length is relatively well simulated. With the increase of the cutting speed (tests 2 and 4), the segment length becomes slightly smaller and consequently, the metric frequency of segmentation becomes more important (Table 6). Moreover, with the use of a negative angle, the segment length is strongly reduced. More precisely, the stiffness degradation in the primary shear zone ensures the chip deformation in a different way as the shear plane shape changes. With a positive rake angle (tests 1 and 2), the shear surface can be described properly by a simple plane in which angle is mainly comprised between 39° and 45° (Fig. 13b and d). By contrast, the use of a negative rake angle gives birth to an additional compression component in the chip during the process which induce deformation in the shear plane and consequently widen

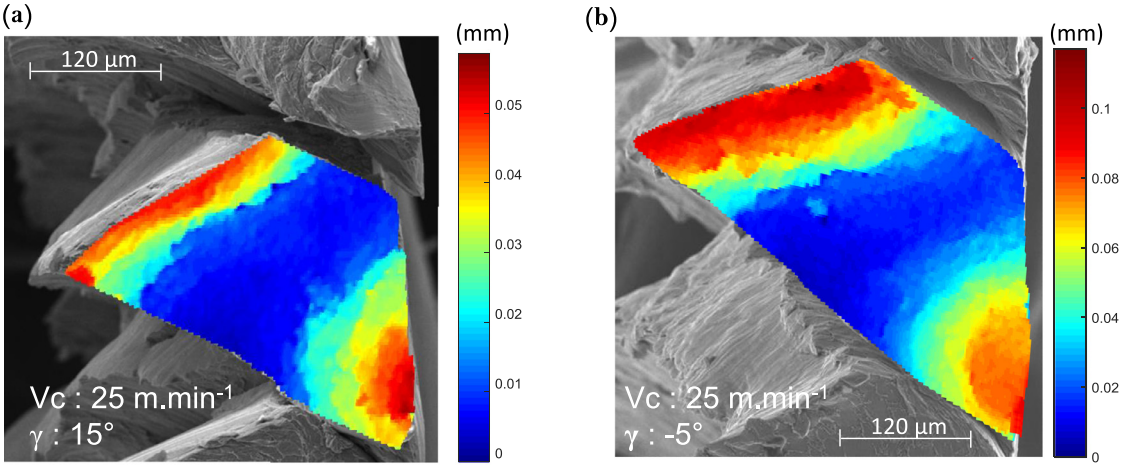

Fig. 12. SEM images of the chips overlaid with the measured altitude map measured by EFCM: (a) test 2 (b) test 4.

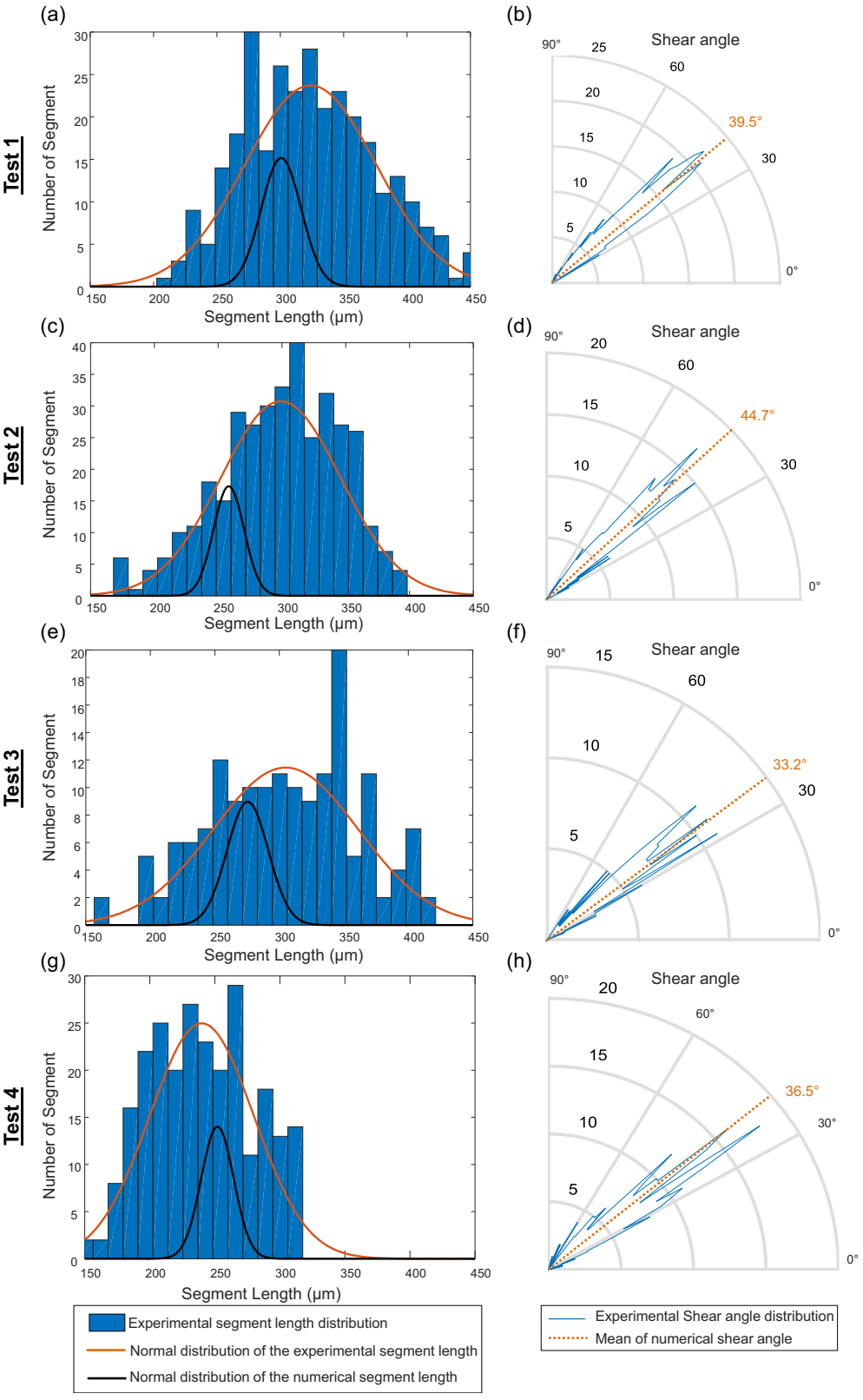

Fig. 13. Segment length and shear angle distributions for each segment.

the dispersion of the shear angle mostly comprised between 30° and 45° (Fig. 13f and h). These experimental findings show the different natures of the mechanical loadings responsible for the material failure in the primary shear zone.

Fig. 14 shows the last computed state of strain before material failure for many points along the primary shear plane.

It can be seen that the loadings that lead to failure differs from the rake angle changes. For a positive rake angle, it is clearly found that shear is leading mode of failure. However, a compressive/shear defor-

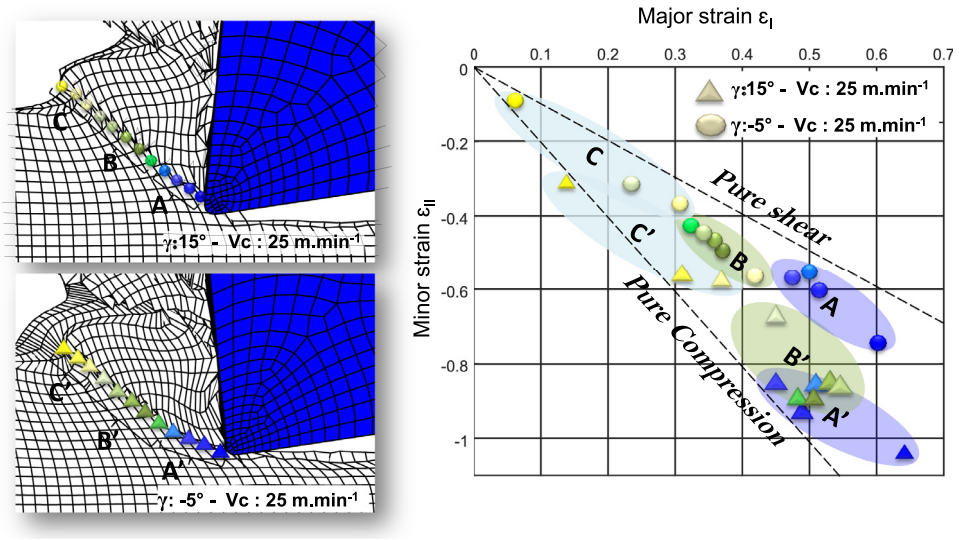

Fig. 14. State of strain at failure in the shear plane for –5° and 15° rake angles.

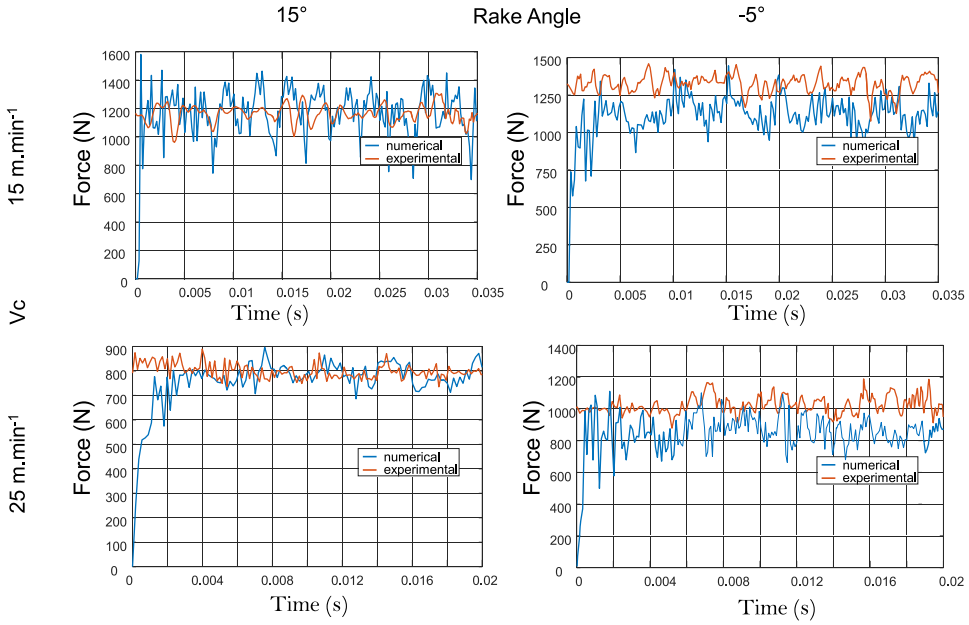

Fig. 15. Experimental and numerical cutting forces comparison for all cutting condition.

mation is observed in the case of the negative rake angle. Nearby the tool tip, the state of the strain is almost strictly compressive while by moving away from the tool tip the shear phenomenon became more and more significant. Multiple conclusions can be drawn from these observations and computations: first, the primary shear zone does not only withstand shear. Second, the nature of the mechanical loading is highly related to the cutting geometry (rake angle) and third the stochastic nature of the observed segment shapes is hardly predicted by computation and further models exhibiting a more probabilistic nature should be added at some point.

Based on these observations, it appears that the shear plane is more hardly affected by the rake angle than by the cutting velocity. Consequently, it tends to prove that the shear angle stays mostly a geometric parameter and thus brings to light several challenges about the influence of the hydrostatic pressure on the shape and geometry of the shear band.

Nevertheless, a great dispersion is observed in the chip parameters (shear angle, length) and in the chip shape throughout tests with a negative rake angle. This highlights the stochastic aspect of the cutting mechanisms and indicates that this aspect seems more important for a negative rake angles.

For all tests, it can be seen that the simulated results present the same order of magnitude than the experimental values. However it is very noticeable that the shape distribution of the computed segments does not exhibit the same variation than the observations. This issue may have two possible origins: (i) the geometric restriction in the Lagrangian finite element model, (ii) the deterministic nature of Finite Elements though numerical instability may lead to some kind of randomness.

5.4. *Cutting forces*

Simulated cutting forces under different machining conditions are presented and compared to experimental data (Fig. 15). It can be noted that the force is affected by the rake angle and the cutting velocity. It increases by varying the rake angle toward negative values or by decreasing the cutting velocity.

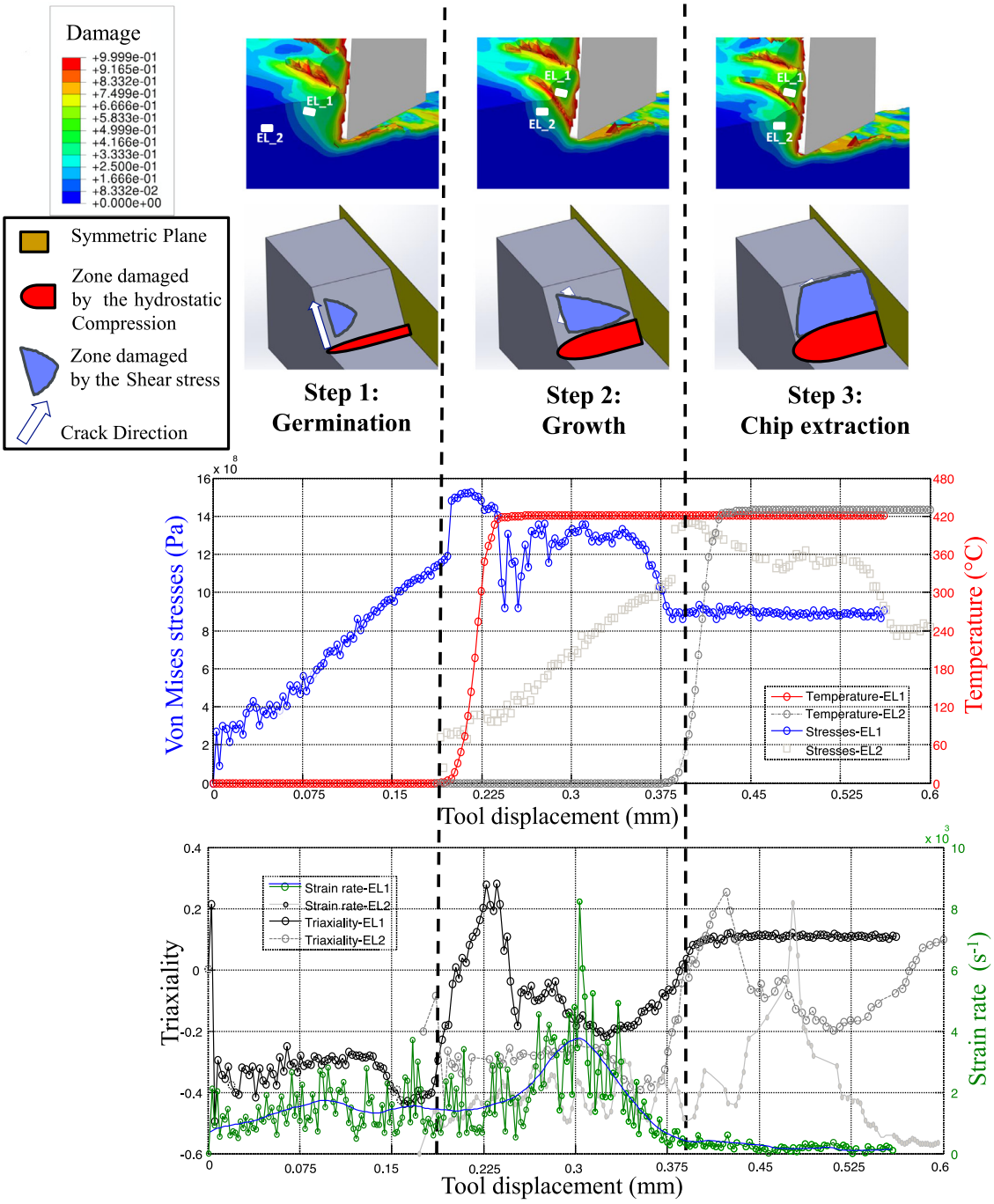

Fig. 16. Steps of the chip formation genesis (Vc: 25 m min^{-1}, rake angle: 15°).

An important variation (up to 500 N) is observed for the numerical forces. It can be explained by many reasons such as the element deletion method, the assumption of a constant cutting velocity, the mesh size.

With a positive rake angle, the measured cutting forces are correctly fitted by the numerical ones. Nerveless, they are slightly underestimated for the negative rake angle. It can be related to the friction coefficient which is constant over all simulations.

In summary, it can be said that simulation results show a good agreement with experiments. It permits to predict the chip formation morphology and the cutting forces under an acceptable error.

5.5. *Chip formation mechanisms*

The use of a reliable Finite Element model allows improving the understanding of serrated chip generation process. More especially, a specific attention is here paid to the chip formation mechanisms. The numerical results presented in Fig. 16 lead to split the chip generation process into three successive steps. This description is backed by the experimental observation presented by Pottier et al. [38] which also proposed to consider three different sub-processes that lead to serrated chips. Indeed, Fig. 16 prompts the evolution of equivalent von Mises stresses, temperature, strain rate and triaxiality ratio during the formation of a single segment. The three successive sub-processes being then:

Table 7
The numerical evolution of the temperature and strain rate over tests.

	$\dot{T}$ (°C μs^{-1})	T_{max} (°C)	$\dot{\varepsilon}_{max}(s^{-1})$
Test 1	123	532	3896
Test 2	308	620	8420
Test 3	145	615	4512
Test 4	348	860	8823

- *Germination:* during this phase, a linear evolution of the von Mises stresses is observed due to a constant compressive loading ($\eta \sim -1/3$) from the tool tip. Elastic energy is stored within the segment (no thermal dissipation is observed) while plasticity develops in the primary shear zone. This loading induces (i) an out of plane deformation of the chip (bulge) also clearly visible on the videos (see Section 4.3) and (ii) a strong hydrostatic compressive zone at the tool tip. The end of this stage is defined by the uprising of a micro crack at the tool tip, i.e. the damage parameter reaches the unity in the first element which is thus deleted.
- *Growth:* it describes the crack evolution along the primary shear plane. It is characterized by a rapid increase of both temperature ($300°C.\mu s^{-1}$) and strain rate (up to 700 s^{-1}). Because of hardening, the von Mises strain remains approximately constant while thermal dissipation is massive (Taylor–Quinney coefficient set to 0.9). The triaxiality ratio passes within the range of [−0.1, 0.1] clearly indicating that shear is the driving mechanisms of this phase. These coupled phenomena activate, firstly the strain accumulation in the shear band (that pushes the segment backward) and secondly the crack propagation along the same direction. This crack starts at the tool tip and evolve inside the shear zone toward the free chip surface as depicted in Fig. 16. The end of this stage is set as the cracks reaches the top surface and no further strain can be summed up into the shear band.
- *Extraction:* the von Mises stress decreases as the segment moves upward along the rake face and leaves the loaded zone. Temperature stabilizes as natural convective–radiative cooling starts (in Fig. 16 temperature remains constant instead of decreasing because adiabatic boundary conditions are prescribed). The damage parameter keeps increasing at the tool/chip interface leading to a slight increase of the hydrostatic compressive zone. The friction upon the next segment leads to a slightly positive triaxiality ratio that remains constant as the strain rate tends toward zero. The segment is then fully formed.

For each numerical test, an element in the chip's segmentation zone was chosen and then, the evolution of temperature $\dot{T}$ (°C μs^{-1}), the maximal temperature T_{max} (°C) and the strain rate $\dot{\varepsilon}_{max}(s^{-1})$ are reported in Table 7. Despite the evolution of the machining conditions (cutting speed and rake angle), it can be underlined that the chip formation mechanisms remain the same. The magnitude of strain rate and temperatures involve changes but the three same sub-processes are observed.

To improve the physical comprehension of the chip formation, complementary chip SEM observations were carried out. As shown in Fig. 17, a material crack is observed in the free side of the chip but is not observed in the stress triaxiality zone. From the observation of Fig. 17b it can be seen that a classical ductile fracture is involve. With another magnification factor, it is observed on the fracture surface that the flow material tends to converge from the side to the center of the cut (Fig. 17c). These observations are consistent with the numerical results presented in the above and confirm the ability of the proposed model to predict the specific kind of fracture involve in segmented chip generation. Nevertheless, these evidences of a ductile fracture do not allow to claim the presence or absence of so-called adiabatic shear bands such as described by Rittel and Wang [49]. It rather seems that both phenomena are consecutive to one another.

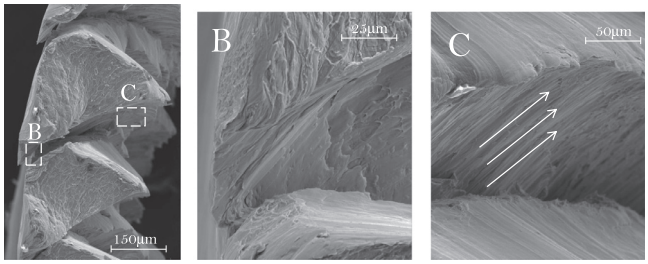

Fig. 17. SEM view of the chip (Vc: 25 m min^{-1}, rake angle 15°), B: detail view of crack, C: detail of crack orientation.

6. Conclusions

This work brings to light the Ti-6Al-4V chip formation problem. The principal aim of this contribution is the comprehension and modeling of the physical phenomena inducing the segmented chip during the machining of the Ti-6Al-4V alloy.

Based on Johnson–Cook model, a new behavior model is proposed to ensure a good description of the tight coupling between the temperature and the strain rate. This model is calibrated by an inverse identification method through dynamic hat-shaped tests performed under different temperatures up to 900 °C and strain rates up to 1000 s^{-1}. The new behavior model properly predicts the experimental data and gives better results than the Johnson–Cook model under all machining conditions.

Since the chip formation results from plastic deformation induced by the shear phenomena, the max shear damage criterion was chosen in this study to describe the ductile fracture during the chip formation. Its Lode angle dependency and its coupled structure to behavior model lead to better description of the damage phenomenon. In addition, it requires only one test for calibration.

A 3D orthogonal cutting model is set up under symmetric hypothesis in order to exhibit the capability of the model in restituting the chip formation mechanisms. In addition, to validate this numerical approach, experimental machining tests using a specific test bench were performed and observed by the mean of a high-speed camera. A good agreement is observed between the numerical and experimental results in terms of cutting forces and chip geometries. Nevertheless, the presented experimental observation leads to consider the chip generation problem as way more stochastic than previously considered in the literature. This very matter should be addressed in future works.

Based on orthogonal cutting simulation results and experimental investigations, it appears that the chip formation process results from a coupled development of both adiabatic shear band and crack propagation which start at the tool tip and evolve inside the shear zone toward the free surface. It can be described by three steps: Germination, Growth and Extraction.

Future works will be focused on in-situ thermal and strain field observation through the use of high speed imaging and infrared thermography, in order to reinforce numerical and the experimental findings. To improve the ability of the proposed model to simulate more accurately the cutting mechanisms, further work has also to be done on the development of a friction law that represents more faithfully the phenomena that occurs in the tool–chip interface and that takes into account the machining parameters.

References

[1] Calamaz M, Limido J, Nouari M, Espinosa C, Coupard D, Salaün M, et al. Toward a better understanding of tool wear effect through a comparison between experiments and SPH numerical modelling of machining hard materials. Int J Refract Met Hard Mater 2009;27:595–604. doi:10.1016/j.ijrmhm.2008.09.005.
[2] Iliescu D, Gehin D, Iordanoff I, Girot F, Gutiérrez ME. A discrete element method for the simulation of CFRP cutting. Compos Sci Technol 2010;70:73–80. doi:10.1016/j.compscitech.2009.09.007.
[3] Komanduri R. Some clarifications on the mechanics of chip formation when machining titanium alloys. Wear 1982;76:15–34. doi:10.1016/0043-1648(82)90113-2.

[4] Nakayama K, Arai M, Kanda T. Machining characteristics of hard materials. CIRP Ann - Manuf Technol 1988;37:89–92 doi:http://dx.doi.org/10.1016/S0007-8506(07)61592-3.

[5] Ayed Y, Germain G, Ben Salem W, Hamdi H. Experimental and numerical study of laser-assisted machining of Ti6Al4V titanium alloy. Finite Elem Anal Des 2014;92:72–9. doi:10.1016/j.finel.2014.08.006.

[6] Liu J, Bai Y, Xu C. Evaluation of ductile fracture models in finite element simulation of metal cutting processes. J Manuf Sci Eng 2013;136:11010. doi:10.1115/1.4025625.

[7] Johnson GR, Cook WH. A constitutive model and data for metals subjected to large strains, high strain rates and high temperatures. In: Proceedings of the 7th International Symposium on Ballistics, vol. 21; 1983. p. 541–7.

[8] Mabrouki T, Courbon C, Zhang Y, Rech J, Nélias D, Asad M, et al. Some insights on the modelling of chip formation and its morphology during metal cutting operations. Comptes Rendus Mécanique 2016;344:335–54. doi:10.1016/j.crme.2016.02.003.

[9] Mabrouki T, Rigal J-F. A contribution to a qualitative understanding of thermo-mechanical effects during chip formation in hard turning. J Mater Process Technol 2006;176:214–21. doi:10.1016/j.jmatprotec.2006.03.159.

[10] Calamaz M, Coupard D, Girot F. A new material model for 2D numerical simulation of serrated chip formation when machining titanium alloy Ti–6Al–4V. Int J Mach Tools Manuf 2008;48:275–88. doi:10.1016/j.ijmachtools.2007.10.014.

[11] Holmquist T, Johnson R. Determination of constants and comparison for various constitutive models. J Phys 1991;4:853–60. doi:10.1051/jp4:19913119.

[12] RULE WK, Jones SE. A revised form for the Johnson–Cook strength model. Int J Impact Eng 1998;21:609–24. doi:10.1016/S0734-743X(97)00081-X.

[13] Woo Jong Kang HH. Crash analysis of auto-body structures considering the strain-rate hardening effect. Seoul: 2000.

[14] Tan JQ, Zhan M, Liu S, Huang T, Guo J, Yang H. A modified Johnson–Cook model for tensile flow behaviors of 7050-T7451 aluminum alloy at high strain rates. Mater Sci Eng A 2015;631:214–19. doi:10.1016/j.msea.2015.02.010.

[15] Khan AS, Sung Suh Y, Kazmi R. Quasi-static and dynamic loading responses and constitutive modeling of titanium alloys. Int J Plast 2004;20:2233–48. doi:10.1016/j.ijplas.2003.06.005.

[16] Vural M, Caro J. Experimental analysis and constitutive modeling for the newly developed 2139-T8 alloy. Mater Sci Eng A 2009;520:56–65. doi:10.1016/j.msea.2009.05.026.

[17] Lin YC, Chen X-M, Liu G. A modified Johnson–Cook model for tensile behaviors of typical high-strength alloy steel. Mater Sci Eng A 2010;527:6980–6. doi:10.1016/j.msea.2010.07.061.

[18] Li H, Wang X, Duan J, Liu J. A modified Johnson Cook model for elevated temperature flow behavior of T24 steel. Mater Sci Eng A 2013;577:138–46. doi:10.1016/j.msea.2013.04.041.

[19] Bäker M. Finite element simulation of high-speed cutting forces. J Mater Process Technol 2006;176:117–26. doi:10.1016/j.jmatprotec.2006.02.019.

[20] Sartkulvanich P, Koppka F, Altan T. Determination of flow stress for metal cutting simulation—a progress report. J Mater Process Technol 2004;146:61–71. doi:10.1016/S0924-0136(03)00845-8.

[21] Andrade UR, Meyers MA, Chokshi AH. Constitutive description of work- and shock-hardened copper. Scr Metall Mater 1994;30:933–8. doi:10.1016/0956-716X(94)90418-9.

[22] Sima M, Özel T. Modified material constitutive models for serrated chip formation simulations and experimental validation in machining of titanium alloy Ti–6Al–4V. Int J Mach Tools Manuf 2010;50:943–60. doi:10.1016/j.ijmachtools.2010.08.004.

[23] McClintock FA. A criterion for ductile fracture by the growth of holes. J Appl Mech 1968;35:363. doi:10.1115/1.3601204.

[24] Rice JR, Tracey DM. On the ductile enlargement of voids in triaxial stress fields∗. J Mech Phys Solids 1969;17:201–17. doi:10.1016/0022-5096(69)90033-7.

[25] Gurson AL. Continuum theory of ductile rupture by void nucleation and growth: part I—Yield criteria and flow rules for porous ductile media. J Eng Mater Technol 1977;99:2–15. doi:10.1115/1.3443401.

[26] Cockcroft MG, Latham DJ. Ductility and the workability of metals. J Inst Met 1968;96:33–9.

[27] Bridgman PW. Studies in large plastic flow and fracture: with special emphasis on the effects of hydrostatic pressure. In: P.W. Bridgman (Ed.). New York-London: McGraw-Hill, 1952. 362 pp. $8.00. Science (80-) 1952;115:424. doi:10.1126/science.115.2990.424.

[28] Johnson GR, Cook WH. Fracture characteristics of three metals subjected to various strains, strain rates, temperatures and pressures. Eng Fract Mech 1985;21:31–48. doi:10.1016/0013-7944(85)90052-9.

[29] Wierzbicki T, Bao Y, Lee Y-W, Bai Y. Calibration and evaluation of seven fracture models. Int J Mech Sci 2005;47:719–43. doi:10.1016/j.ijmecsci.2005.03.003.

[30] Wilkins ML, Streit RD, Reaugh JE. Cumulative-strain-damage model of ductile fracture: simulation and prediction of engineering fracture tests. Lawrence Livermore Natl Lab CA (USA), Sci Appl Inc, San Leandro, CA, Tech Report, UCRL-53058 1980.

[31] Wierzbicki T, Xue L. On the effect of the third invariant of the stress deviator on ductile fracture; Impact Crashworthiness Lab Tech Rep; 2005.

[32] Ludwik P. Elemente Der Technologischen Mechanik. Wien, Deutschland: 1909. doi:10.1007/978-3-662-40293-1.

[33] Germain G, Morel A, Braham-Bouchnak T. Identification of material constitutive laws representative of machining conditions for two titanium alloys: Ti6Al4V and Ti555-3. J Eng Mater Technol 2013;135:31002–11.

[34] Hor A, Morel F, Lebrun J-L, Germain G. Modelling, identification and application of phenomenological constitutive laws over a large strain rate and temperature range. Mech Mater 2013;64:91–110. doi:10.1016/j.mechmat.2013.05.002.

[35] Harzallah M, Pottier T, Senatore J, Mousseigne M, Germain G, Landon Y. A new behavior model for better understanding of titanium alloys Ti-6Al-4V chip formation in orthogonal cutting. AIP Conf Proc, 1769; 2016. doi:10.1063/1.4963490.

[36] Marquardt DW. An algorithm for least-squares estimation of nonlinear parameters. J Soc Ind Appl Math 1963;11:431–41. doi:10.1137/0111030.

[37] Ponthot JP, Kleinermann JP. A cascade optimization methodology for automatic parameter identification and shape/process optimization in metal forming simulation. Comput Methods Appl Mech Eng 2006;195:5472–508. doi:10.1016/j.cma.2005.11.012.

[38] Pottier T, Germain G, Calamaz M, Morel A, Coupard D. Sub-millimeter measurement of finite strains at cutting tool tip vicinity. Exp Mech 2014;54:1031–42. doi:10.1007/s11340-014-9868-0.

[39] Malvern LE. Introduction to the mechanics of a continuous medium. 1969.

[40] Bai Y, Wierzbicki T. Application of extended Mohr-Coulomb criterion to ductile fracture. Int J Fract 2010;161:1–20. doi:10.1007/s10704-009-9422-8.

[41] Bao Y, Wierzbicki T. On the cut-off value of negative triaxiality for fracture. Eng Fract Mech 2005;72:1049–69. doi:10.1016/j.engfracmech.2004.07.011.

[42] Ben Abdelali H, Claudin C, Rech J, Ben Salem W, Kapsa P, Dogui A. Experimental characterization of friction coefficient at the tool-chip-workpiece interface during dry cutting of AISI 1045. Wear 2012;286–287:108–15. doi:10.1016/j.wear.2011.05.030.

[43] Abaqus Abaqus Documentation 6.13, ; 2013. http://129.97.46.200:2080/v6.13/

[44] Puls H, Klocke F, Lung D. Experimental investigation on friction under metal cutting conditions. Wear 2014;310:63–71. doi:10.1016/j.wear.2013.12.020.

[45] Zorev N. Interrelationship between shear processes occurring along tool face and on shear plane in metal cutting. In: ASME Proc Int Res Prod Eng. New York; 1963. p. 42–9.

[46] Zhang Y, Outeiro JC, Mabrouki T. On the selection of Johnson–Cook constitutive model parameters for Ti-6Al-4V using three types of numerical models of orthogonal cutting. Proc CIRP 2015;31:112–17. doi:10.1016/j.procir.2015.03.052.

[47] Atlati S, Haddag B, Nouari M, Zenasni M. Analysis of a new segmentation intensity ratio “SIR” to characterize the chip segmentation process in machining ductile metals. Int J Mach Tools Manuf 2011;51:687–700. doi:10.1016/j.ijmachtools.2011.05.007.

[48] Ducobu F, Rivière-Lorphèvre E, Filippi E. Numerical contribution to the comprehension of saw-toothed Ti6Al4V chip formation in orthogonal cutting. Int J Mech Sci 2014;81:77–87. doi:10.1016/j.ijmecsci.2014.02.017.

[49] Rittel D, Wang ZG. Thermo-mechanical aspects of adiabatic shear failure of AM50 and Ti6Al4V alloys. Mech Mater 2008;40:629–35. doi:10.1016/j.mechmat.2008.03.002.